19. Names have been assigned to geographic features by the Mars Exploration Rover (MER) team for planning and operations purposes. They are not formally recognized by the International Astronomical Union.
20. The Challenger Memorial Station was named to honor the crew of the Space Shuttle *Challenger*, who perished on 28 January 1986. The name Challenger Memorial Station refers both to the lander itself and to the martian terrain that it occupies.
21. R. E. Arvidson *et al.*, *Science* **306**, 1730 (2004).
22. L. A. Soderblom *et al.*, *Science* **306**, 1723 (2004).
23. R. Rieder *et al.*, *Science* **306**, 1746 (2004).
24. G. Klingelhöfer *et al.*, *Science* **306**, 1740 (2004).
25. K. E. Herkenhoff *et al.*, *Science* **306**, 1727 (2004).
26. P. R. Christensen *et al.*, *Science* **306**, 1733 (2004).
27. J. F. Bell III *et al.*, *Science* **306**, 1703 (2004).
28. S. W. Squyres *et al.*, *Science* **306**, 1709 (2004).
29. P. W. Choquette, L. C. Pray, *Am. Assoc. Petrol. Geol. Bull.* **54**, 207 (1970).
30. J. C. Harms, J. B. Southard, R. G. Walker, *Structures and Sequences in Clastic Rocks* (Society of Economic Paleontologists and Mineralogists, Tulsa, OK, 1982).
31. G. V. Middleton, J. B. Southard, *Mechanics of Sediment Movement* (Society of Economic Paleontologists and Mineralogists, Providence, RI, 1984).
32. J. B. Southard, J. A. Boguchwal, *J. Sed. Petrol.* **66**, 680 (1990).
33. A. Banin, B. C. Clark, H. Wänke, in *Mars*, H. H. Kieffer, B. M. Jakosky, C. W. Snyder, M. S. Matthews, Eds. (Univ. of Arizona Press, Tucson, AZ, 1992), pp. 584–625.
34. P. R. Christensen, R. V. Morris, M. D. Lane, J. L. Bandfield, M. C. Malin, *J. Geophys. Res.* **106**, 23 (2001).
35. P. R. Christensen, S. W. Ruff, *J. Geophys. Res.* **109**, E08003 (2004).
36. M. D. Smith *et al.*, *Science* **306**, 1750 (2004).
37. M. D. Smith, *Icarus* **167**, 148 (2004).
38. M. T. Lemmon *et al.*, *Science* **306**, 1753 (2004).
39. R. E. Arvidson *et al.*, *J. Geophys. Res.* **108**, 8073 (2003).
40. We are deeply indebted to the many hundreds of engineers and scientists—far too numerous to name here—who made the MER Project and the Athena Science Investigation possible. Funding for the MER Project, including most of the Athena Payload, was provided by NASA. The APXS and Mössbauer instruments were funded by the German space agency (DLR), and the magnet array was funded by the Danish government. A portion of the research described in this paper was carried out at the Jet Propulsion Laboratory, California Institute of Technology, under a contract with NASA. The MER Project was led with skill and dedication by P. Theisinger, and the development of the MER flight system was led with equal skill and dedication by R. Cook and B. Goldstein. J. Rademacher managed the development of the Mini-TES, APXS, and Mössbauer payload elements, M. Schwochert led the engineering teams for Pancam and the Microscopic Imager, and S. Kondos and M. Johnson managed the development of the RAT. To all of them, and to the hundreds of members of the MER family who have made this adventure such a joy and privilege to be part of, we express our heartfelt and lasting thanks.

Plates Referenced in Article
www.sciencemag.org/cgi/content/full/306/5702/1698/DC1
Plates 3 to 7, 9, 10, and 12 to 16

7 October 2004; accepted 2 November 2004

RESEARCH ARTICLE

Pancam Multispectral Imaging Results from the Opportunity Rover at Meridiani Planum

J. F. Bell III,[1*] S. W. Squyres,[1] R. E. Arvidson,[2] H. M. Arneson,[1] D. Bass,[3] W. Calvin,[4] W. H. Farrand,[5] W. Goetz,[6] M. Golombek,[3] R. Greeley,[7] J. Grotzinger,[8] E. Guinness,[2] A. G. Hayes,[1] M. Y. H. Hubbard,[1] K. E. Herkenhoff,[9] M. J. Johnson,[1] J. R. Johnson,[9] J. Joseph,[1] K. M. Kinch,[10] M. T. Lemmon,[11] R. Li,[12] M. B. Madsen,[6] J. N. Maki,[3] M. Malin,[13] E. McCartney,[1] S. McLennan,[14] H. Y. McSween Jr.,[15] D. W. Ming,[16] R. V. Morris,[16] E. Z. Noe Dobrea,[1] T. J. Parker,[3] J. Proton,[1] J. W. Rice Jr.,[7] F. Seelos,[2] J. M. Soderblom,[1] L. A. Soderblom,[9] J. N. Sohl-Dickstein,[1] R. J. Sullivan,[1] C. M. Weitz,[17] M. J. Wolff[5]

Panoramic Camera (Pancam) images from Meridiani Planum reveal a low-albedo, generally flat, and relatively rock-free surface. Within and around impact craters and fractures, laminated outcrop rocks with higher albedo are observed. Fine-grained materials include dark sand, bright ferric iron–rich dust, angular rock clasts, and millimeter-size spheroidal granules that are eroding out of the laminated rocks. Spectra of sand, clasts, and one dark plains rock are consistent with mafic silicates such as pyroxene and olivine. Spectra of both the spherules and the laminated outcrop materials indicate the presence of crystalline ferric oxides or oxyhydroxides. Atmospheric observations show a steady decline in dust opacity during the mission. Astronomical observations captured solar transits by Phobos and Deimos and time-lapse observations of sunsets.

On 24 January 2004 UTC, the Mars Exploration Rover Opportunity landed on Mars within the classical low-albedo Noachian terrain of Meridiani Planum. The landing region was previously identified in orbital remote sensing data as being flat-lying layered and/or etched materials characterized by an unusual surficial concentration of coarse-grained gray hematite at the 15 to 20% areal abundance level (*1*–*3*). The lander and encapsulated rover came to rest inside an impact crater, 3 m deep and 20 m in diameter, informally known as Eagle crater (*4*). Using the Pancam charge-coupled device (CCD) imaging system (*5*, *6*), we acquired high spatial resolution multispectral panoramic images of the landing site and its environs to characterize the morphology, composition, and physical and atmospheric properties of the region.

Pancam images were calibrated using preflight laboratory measurements and then converted to I/F (where I = measured scene radiance and πF = the solar irradiance at the top of the martian atmosphere), which is reflectance relative to the onboard Pancam calibration target, corrected for solar incidence angle and dust deposition effects (*5*–*7*). During Opportunity's 90-sol primary mission, more than 8900 Pancam images were acquired and downlinked. These images include two 360° 5- and 6-color stereo panoramas from inside Eagle crater and on the plains just outside the crater, four 7-color stereo mosaics covering the Eagle crater outcrop at high resolution, more than 100 11-color multispectral spot observations of trenches, Rock Abrasion Tool (RAT) drill holes and other rock and soil (*8*, *9*) regions of interest within Eagle crater and during the traverse across the plains, and photometric imaging sequences designed to

[1]Department of Astronomy, Cornell University, Ithaca NY 14853, USA. [2]Department of Earth and Planetary Sciences, Washington University, St. Louis, MO 63130, USA. [3]Jet Propulsion Laboratory, California Institute of Technology, Pasadena, CA 91109, USA. [4]Department of Geological Sciences, University of Nevada, Reno, NV 89501, USA. [5]Space Science Institute, Boulder, CO 80301, USA. [6]University of Copenhagen, DK-2100 Copenhagen Ø, Denmark. [7]Department of Geological Sciences, Arizona State University, Tempe, AZ 85287, USA. [8]Department of Earth, Atmospheric, and Planetary Sciences, Massachusetts Institute of Technology, Cambridge, MA 02139, USA. [9]U.S. Geological Survey, Flagstaff, AZ 86001, USA. [10]Aarhus University, DK-8000 Aarhus C, Denmark. [11]Department of Atmospheric Sciences, Texas A&M University, College Station, TX 77843, USA. [12]Department of Civil and Environmental Engineering and Geodetic Science, Ohio State University, Columbus, OH 43210, USA. [13]Malin Space Science Systems Inc., San Diego, CA 92191, USA. [14]Department of Geosciences, State University of New York, Stony Brook, NY 11794, USA. [15]Department of Earth and Planetary Sciences, University of Tennessee, Knoxville, TN 37996, USA. [16]NASA Johnson Space Center, Houston, TX 77058, USA. [17]Planetary Science Institute, Tucson, AZ 85719, USA.

*To whom correspondence should be addressed. E-mail: jfb8@cornell.edu

provide information on surface physical properties and albedo and to facilitate comparisons between orbital remote sensing observations and ground truth.

Physiographic observations. The initial panoramic views of the Opportunity landing site concentrated on the interior of Eagle crater (Plate 1). The interior of Eagle crater has a surface area of ~350 m^2 and is dominated by dark reddish-brown, fine-grained, unconsolidated debris. Preserved indentation and disturbance patterns generated by the impact and retraction of the lander airbags (Fig. 1) and observations of wheel tracks and trench wall slopes (*10*) (Plates 14 to 16) indicate that this debris is weakly cohesive.

Two new classes of martian surface materials were discovered inside the crater. One class consists of high-albedo, yellowish-red outcrop about halfway up the inside of the crater wall (Plates 1 and 13, the latter of which shows a ~10-m-long section of the northern part of the outcrop) in the western and northern half of the crater. Outcrop exposures are ~50 cm high by 30 m wide; some are flush with the crater wall, and others protrude ~30 cm above the fine-grained debris that covers the floor and wall of the crater. The outcrop consists of indurated or lithified materials, some of which exhibit subcentimeter-scale laminations (*11*) (Fig. 2) (Plates 6 and 7). Some of the large-scale bedding exhibits juxtaposed strike and dip angles, suggesting that the outcrop may have been faulted or disrupted by the impact process (*11*). The second class consists of a population of millimeter- to subcentimeter-sized dark, spherical granules (spherules) found heterogeneously distributed within the crater. Some of the spherules are embedded in or eroding from the outcrop (*12*) (Fig. 3), which suggests that the origin of the spherules is intimately tied to the origin of the outcrop material.

Observations of the plains made immediately after Opportunity left Eagle crater on sol 57 (*13*) show a flat (~10 cm relief or less), dark terrain with only one large rock and a few small pebbles visible out to the horizon (Plate 2). A pattern of brighter, redder streaks on the plains is interpreted as wind ripples (*12*) that follow a dominantly northwest-southeast trend throughout the region in orbital images (*2*, *3*, *14*). Shallow linear depressions and other small, roughly circular craters and depressions, similar to features observed throughout the region from Mars Global Surveyor (MGS) high-resolution orbital images, are also visible in Pancam

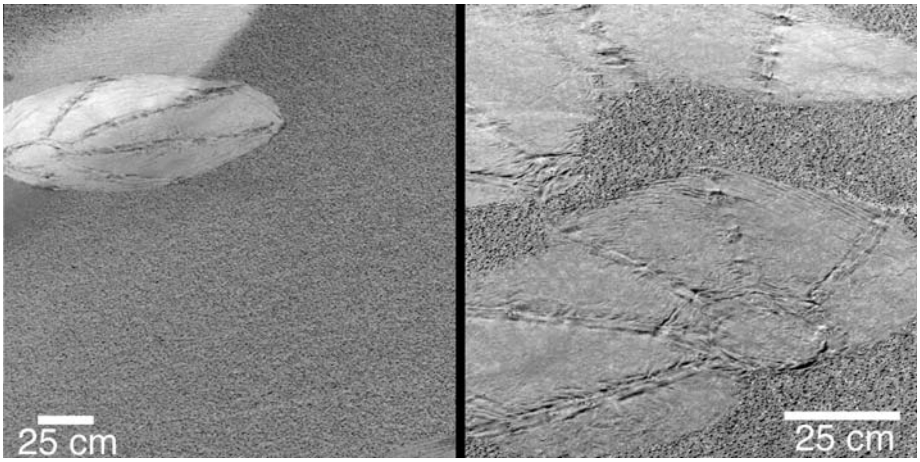

Fig. 1. Pancam images of imprint marks left in the soil as the airbag-shrouded lander came to a rest within Eagle crater. Left: Pancam 750-nm filter image from sol 3, sequence P2213, acquired at 11:22 LTST (*13*). Right: Pancam 750-nm filter image from sol 2, sequence P2217, acquired at 13:41 LTST.

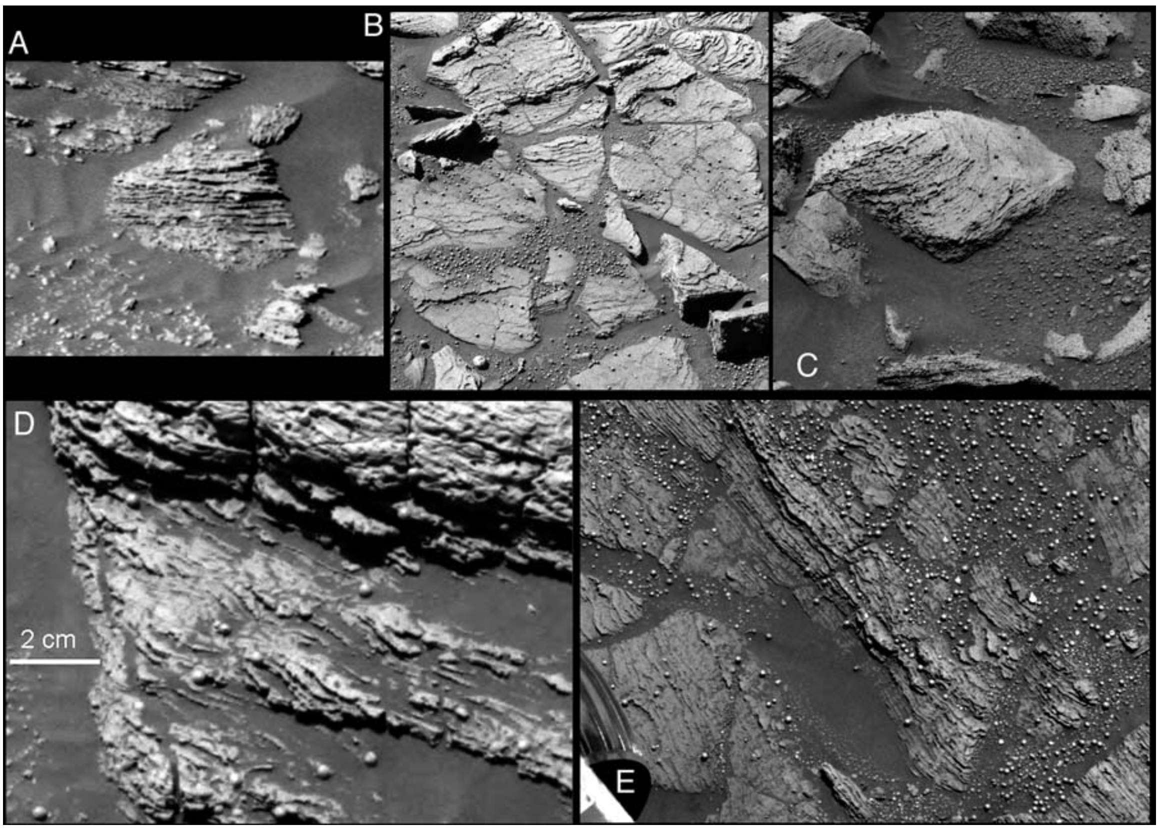

Fig. 2. Examples of laminated, spherule-bearing outcrop deposits in Pancam images, from 430-nm filter images. (**A**) Unnamed 12-cm-wide rock from sol 16, sequence P2260, in Eagle crater. (**B**) An 80-cm-wide part of Shoemaker's Patio from sol 49, sequence P2400, in Eagle crater. (**C**) The 20-cm-wide rock Pilbara from sol 85, sequence P2532, near Fram crater. (**D**) Part of the rock Last Chance from sol 38, sequence P2538, in Eagle crater. (**E**) An 80-cm-wide part of the rock Slickrock from sol 43, sequence P2555, in Eagle crater. Opportunity's front left wheel can be seen at lower left.

images of the plains. During the traverse to Endurance crater (Plate 5), the rover obtained images of one of the linear depressions, called Anatolia, showing outcrop similar in color and texture to the outcrop in Eagle crater (Fig. 4). The shallow impact crater called Fram, 8 m in diameter, also contains outcrop similar to that in Eagle crater (Plate 4).

The color properties, the ubiquitous presence of fine lamination and spherules within bright outcrop at Eagle, Anatolia, Fram, and Endurance, and the independent compositional evidence for uniformly high sulfur and jarosite $[(K,Na)Fe_3(SO_4)_2(OH)_6]$ in the outcrop (*15*, *16*) all suggest that the substrate materials are laterally continuous and support the interpretation that the outcrop is a widespread deposit formed in liquid water (*11*). In this region of Meridiani Planum, this ancient sedimentary unit is buried beneath relatively thin (~1 m) deposits of darker sand, spherules, and dust.

Rocks and fine-grained materials. High-resolution Pancam images of clastic materials within Eagle crater and in the plains of Meridiani reveal distinct populations of materials based on morphology, color, and other properties (Fig. 5). Fine-grained materials include dark sand and brighter dust deposits. Where disturbed by airbags or the rover's wheels, these materials are observed to darken in brighter regions and to redden in darker regions. The darkening is probably a result of excavation of slightly coarser grains that underlie a thin, fine-grained ferric iron–rich surface layer, similar to disturbed surfaces at the Viking and Mars Pathfinder landing sites. The reddening is probably the result of burial and/or dispersal of coarse-grained ferric iron–rich materials such as the spherules. Clastic grains include bright and dark granules; some are spherical and range in size from ~1 to 5 mm, whereas others are angular and range in size from ~1 mm to 10 cm (*17*). There is a bimodal distribution of fine-grained materials, consisting of the 1- to 5-mm granules visible to Pancam and very fine sand (<100 μm) visible to the Microscopic Imager (MI) (*12*), and a lack of fine, medium, and coarse sand (~125 to 800 μm).

Larger rocky materials at the site are limited to the outcrop deposits seen at Eagle (Fig. 2), Anatolia (Fig. 4), Fram (Plate 4), Endurance, and (rarely) rocks seen elsewhere in the plains (Plate 12) (*12*). The outcrop remained intact after being scuffed and driven over by the rover wheels (Fig. 5, C and D), which supports the interpretation that it is a lithified unit rather than weakly indurated soil deposits (*10*).

Photometric observations. Calibrated Pancam images acquired on sol 22 with the broadband filter (L1, 739 ± 338 nm bandpass) were used to estimate the albedo (*18*) of the dark deposits within Eagle crater to be 0.14 ± 0.01. This is comparable to the average albedo of the plains outside of Eagle crater, estimated to be 0.12 ± 0.01 on the basis of L1 imaging measurements on sol 68. These albedos are comparable to the Viking Orbiter Infrared Thermal Mapper bolometric albedo (0.14 ± 0.06) and to the MGS Thermal Emission Spectrometer (TES) bolometric albedo (0.12 ± 0.03) of the Opportunity landing site pixel, which is in a lower-than-average albedo portion of the landing ellipse (*2*). The bright outcrop materials within Eagle crater exhibit an average albedo of 0.25 ± 0.06, and brighter wind streak deposits within and surrounding Eagle crater exhibit albedo values between 0.19 and 0.29, consistent with the albedo of bright dust.

We acquired images of surface features within Eagle crater and the plains at different times of day to document reflectance variations related to physical properties such as texture, grain size, and porosity (*19*, *20*). Examples include images targeted along the photometric equator, both within Eagle crater and in the plains east of Fram crater, and images targeted to monitor variations within specific regions of spherules and rock clasts (Fig. 6). Although much of the surface exhibits approximately Lambertian photometric behavior, the spherules and some clasts exhibit strong specular glints that suggest smooth and/or indurated surfaces. Several of these photometric sequences were timed to coordinate with down-looking observations

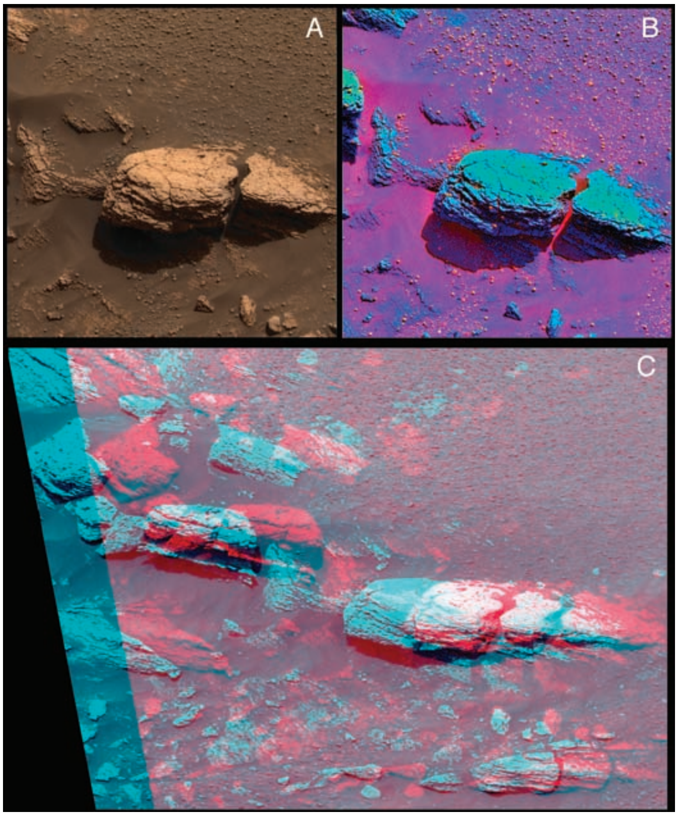

Fig. 3. Sol 13 and 14 Pancam images of the northeast end of the Eagle crater outcrop. (**A**) Approximate true-color rendering of the rock Stone Mountain, 16 cm high by 35 cm wide, acquired on sol 14 from sequence P2550 and generated with Pancam's left eye 600-, 530-, and 480-nm filters. (**B**) False-color composite from the same sequence as in (A) but generated with Pancam's right eye filters, with red = the 430- to 750-nm color ratio, green = *I/F* at 430 nm, and blue = the 900- to 1030-nm color ratio. (**C**) Stereo anaglyph image of this region of the Eagle crater outcrop, for viewing with red/blue stereo glasses. Images were acquired on sol 13 as part of sequence P2376.

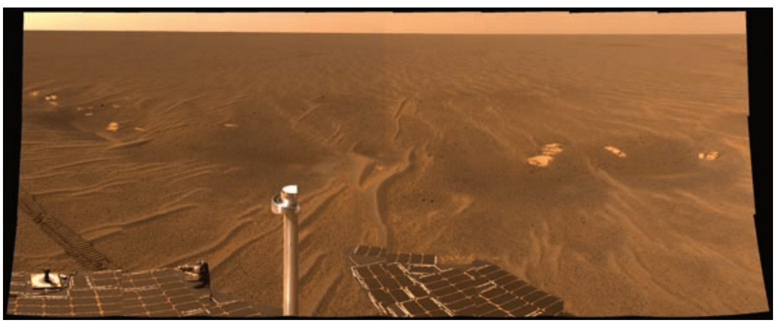

Fig. 4. Pancam color mosaic of the linear depression known as Anatolia, from sol 71, sequences P2281 and P2282. The part of the feature seen here is ~12 m wide. This is an approximate true-color rendering generated with Pancam's 750-nm filter for red, 480-nm filter for blue, and an average of those two filters as a synthesized green channel.

of the landing site during spacecraft overflights by the Mars Odyssey, Mars Express, and MGS orbiters [e.g., (*21*)].

Multispectral observations. Multispectral images were frequently used to identify potentially distinct compositional and mineralogic units and trends within outcrop and plains materials and to help guide the choice of specific targets for detailed in situ investigation with the rover's arm instruments. Targeted 11-color Pancam multispectral observations identified unique visible to near-infrared (IR) spectral units within Eagle crater and during the plains traverse to Endurance crater (Figs. 7 and 8). These units include bright and dark versions of soils, granules, rock clasts, and outcrop materials; larger dark rocks; regions of soil and rock disturbed by airbag, rover wheel, or RAT actions; and the sky.

The spectra provide constraints on the iron-bearing mineralogy of the materials exposed at the site. For example, outcrop materials in Eagle crater and elsewhere (Fig. 7; Fig. 8, A and E) exhibit a strong and relatively smooth near-ultraviolet to visible reflectance increase that is consistent with the presence of ubiquitous, fine-grained, perhaps nanophase (*22*) ferric iron–bearing iron oxide. Physical properties experiments (*10*) (Fig. 5, C and D) indicate that the fine-grained ferric iron material is not eolian dust covering the outcrop rocks. Spectra of the outcrop in Eagle crater were used to search for and identify other outcrop deposits in observations of the plains and distant drive targets (e.g., Figs. 4, 7E, and 8E) (Plate 4).

Most dark sand and other dark Eagle crater floor and Meridiani plains materials also exhibit a ferric iron spectral signature, but in contrast to the outcrop, their spectra show stronger evidence of crystalline ferrous or ferric iron–bearing phases (Fig. 7; Fig. 8, A, B, and E). Specifically, a stronger kink in the spectra near 530 nm and a shallow absorption band centered near 900 to 950 nm are consistent with ferric iron–bearing phases such as schwertmannite, ferrihydrite, and disordered goethite [e.g., (*23*, *24*)]. Although the 900- to 950-nm band is not consistent with the presence of fine-grained, crystalline ("red") hematite alone, the presence of that band and the kink at 530 nm may indicate a mixture of red hematite and (i) a ferric iron–bearing phase such as the hydroxide sulfate phase jarosite, (ii) a ferric oxyhydroxide such as goethite, or (iii) a ferrous iron–bearing volcanic phase such as pyroxene (*25*–*27*). The dark Eagle crater floor and Meridiani plains materials are observed to brighten and redden where compacted by the lander's airbags (e.g., Figs. 7B and 8B); such spectral behavior is consistent with either the creation of finer grained ferric iron phases from crushing and/or disaggregation of coarser phases, or the preferential burial of the coarser grained ferric iron materials during the compaction event. The latter interpretation is supported by MI imaging (*12*).

Small granules, rock clasts, and rare dark rocks exhibit a range of spectral diversity in the visible to near-IR range (e.g., Figs. 6, 7C, and 8C). Spectra of individual dark spherules

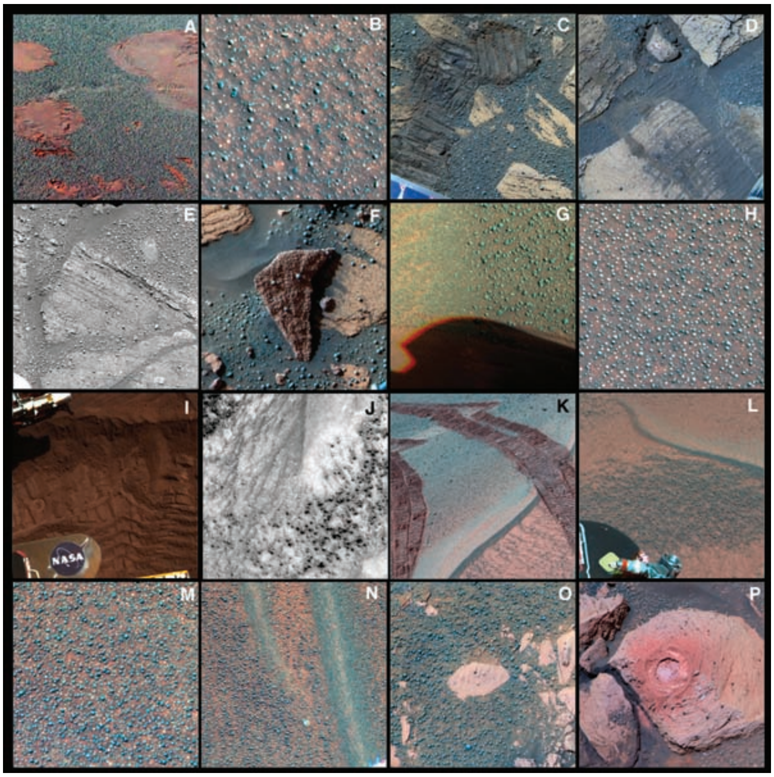

Fig. 5. Examples of color and morphologic diversity observed at Pancam's highest spatial resolution during Opportunity's first 90 sols. The features are ~1.6 m from the camera; each image is ~40 to 50 cm across. The smallest features visible in the images are ~0.8 to 1.0 mm across. (**A**) Sol 2, sequence P2218. (**B**) Sol 17, sequence P2555. (**C**) Sol 37, sequence P2534. (**D**) Sol 37, sequence P2535. (**E**) Sol 43, sequence P2554. (**F**) Sol 49, sequence P2571. (**G**) Sol 53, sequence P2599. (**H**) Sol 54, sequence P2530. (**I**) Sol 55, sequence P2403. (**J**) Sol 59, sequence P2558. (**K**) Sol 60, sequence P2211. (**L**) Sol 60, sequence P2217. (**M**) Sol 63, sequence P2572. (**N**) Sol 73, sequence P2589. (**O**) Sol 85, sequence P2533. (**P**) Sol 88, sequence P2542, post-RAT drilling. Images were generated with the 430-nm filter alone (E) or the 750-nm filter alone (J), or are false-color composites generated with the 750-, 530-, and 480-nm filters [(A), (K), and (L)], 750-, 530-, and 430-nm filters [(B), (F) to (H), and (M) to (P)], or 600-, 530-, and 430-nm filters [(C) and (D)]. (I) is an approximate true-color composite generated with the 600-, 530-, and 480-nm filters.

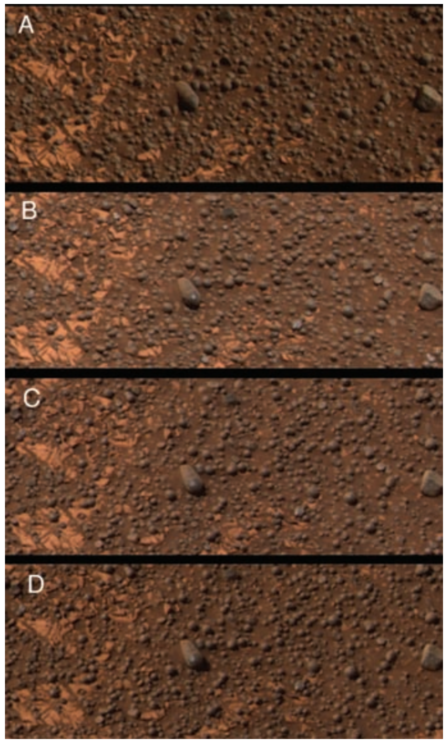

Fig. 6. Example of Pancam images from four times of day, showing differences in brightness and color of a patch of dark soil, spherules, rock clasts, and pieces of bright outcrop in Eagle crater. Each image is an approximate true-color rendering generated from Pancam's 600-, 530-, and 480-nm filters, and all are stretched to the same contrast and color level. The scene is ~50 cm across; the smallest grains visible in the images are ~1 mm in size. (**A**) Sol 32, sequence P2581, 09:20 LTST; illumination from upper right. (**B**) Sol 30, sequence P2579, 11:51 LTST; illumination from just right of center. (**C**) Sol 29, sequence P2575, 13:19 LTST; illumination from just left of center. (**D**) Sol 32, sequence P2587, 14:01 LTST; illumination from upper left.

from Eagle crater (Figs. 6 and 8F) (Plate 11) exhibit crystalline ferric iron spectral signatures similar to those seen in the dark Eagle crater soils and Meridiani plains. Color ratio images of Pancam filters R7 and R6 (1009 nm/934 nm) and other similar parameterizations (*9*) provide a quick way to map the distribution of spherules and indicate that they are ubiquitous across the part of the Meridiani plains imaged by Pancam. Some areas within Eagle crater have partially buried spherules that have a higher albedo of 0.20 to 0.25. Spectra of these higher albedo spherules are consistent with low-albedo spherules covered or coated by high-albedo nanocrystalline ferric iron–rich dust. In areas where the RAT ground into spherules embedded in the outcrop (e.g., Plates 9 to 11, which show examples of the 4.5-cm-diameter RAT holes), the RAT cuttings are redder than the unabraded rock surfaces and exhibit 11-color spectra consistent with the presence of fine-grained ferric iron oxides. These observations, combined with Miniature Thermal Emission Spectrometer (Mini-TES) and Mössbauer spectrometer identification of hematite signatures within spherule-rich regions (*16*, *28*), indicate that the spherules and their fragments are a carrier of the crystalline gray hematite observed from orbit in this region of Mars (*1*). However, similar crystalline ferric iron spectral signatures are also seen in Pancam spectra of some dark rock clasts and soil deposits (Fig. 7; Fig. 8, A, C, and F), implying that the spherules may not be the only carrier of the hematite in this region (*17*).

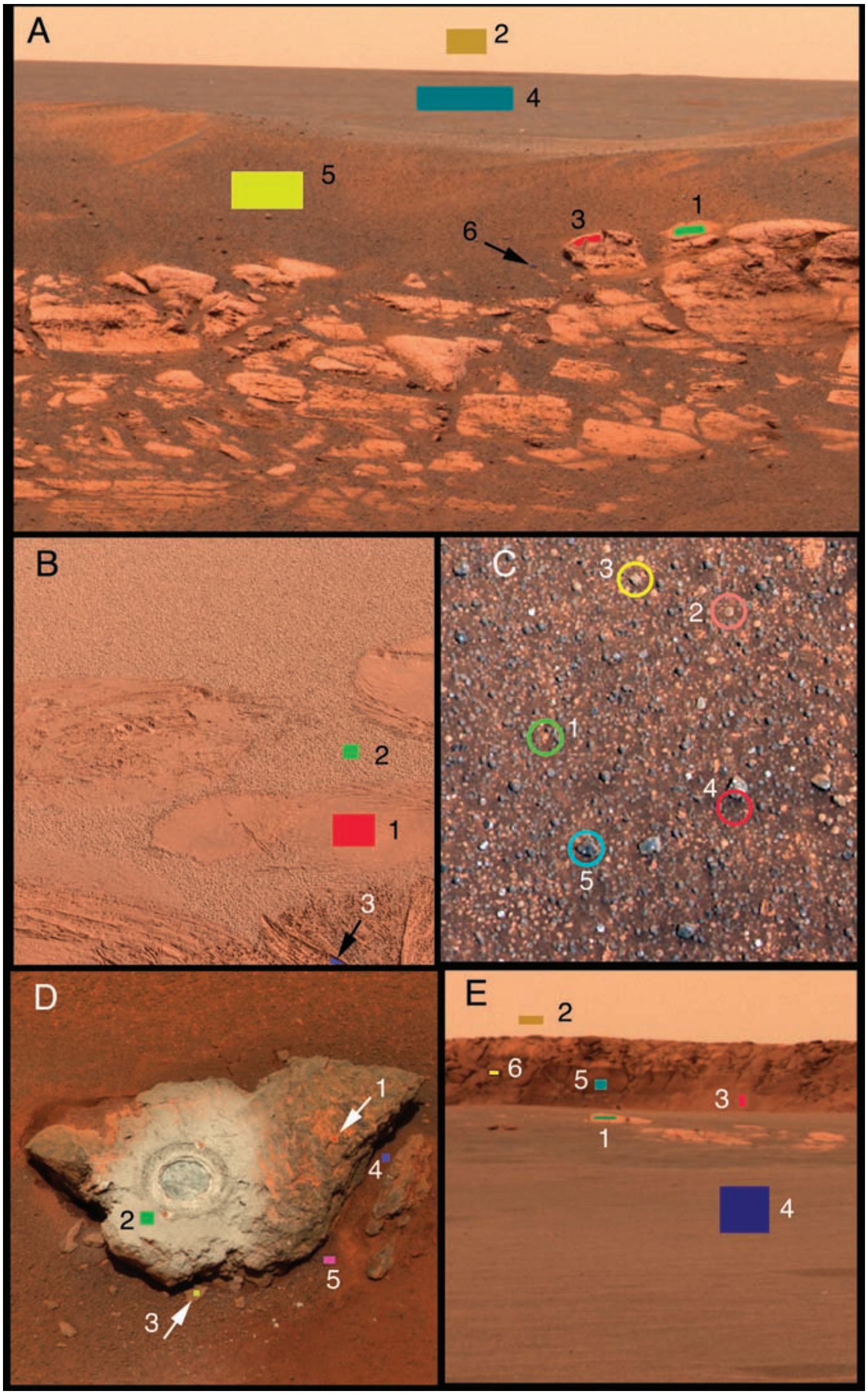

Fig. 7. Examples of regions chosen for detailed Pancam multispectral observations. Spectra extracted from the colored boxes are shown in Fig. 8. (**A**) A 3-m-wide region of the outcrop in Eagle crater: sol 4, sequence P2353. (**B**) Airbag bounce and drag marks within a 1.6-m-wide region of Eagle crater: sol 3, sequence P2530. (**C**) A 50-cm-wide region of soil and rock clast deposits in Eagle crater: sol 20, sequence P2564. (**D**) A 40-cm-wide Bounce rock in the plains outside of Eagle crater: sol 68, sequence P2581. (**E**) View across the plains at the eastern wall of Endurance crater: sol 94, sequence P2556. The rock at point 1 is ~75 cm wide and ~70 m away. All images are approximate true-color renderings generated using Pancam's 600-, 530-, and 480-nm filters.

Some small dark rock clasts within Eagle crater, as well as dust-free surfaces of Bounce rock exposed by grinding, exhibit a negative spectral slope from 750 to 1000 nm and/or a strong near-IR absorption band centered near 1000 nm or at a longer wavelength (Fig. 7; Fig. 8, C and D). These features are consistent with the presence of ferrous iron–bearing silicate phases such as pyroxene or olivine (*29*–*32*). In situ analysis by the Mössbauer spectrometer showed the presence of one or more pyroxene phases in Bounce rock, and also showed that olivine was negligible (*16*). Abundant pyroxene but only minor amounts of olivine were also identified in this rock on the basis of Mini-TES measurements (*28*).

Trenches ~16 cm wide by ~150 cm long by 5 to 10 cm deep were dug by the rover wheels in Eagle crater and in the plains near Anatolia (Plates 14 to 16). Multispectral images of these trenches show that the shallow subsurface has fewer spherules and rock clasts than the surface. Trench walls and excavated piles are slightly redder than surrounding untrenched materials. These observations support the interpretation of these surfaces as a deflationary lag or pavement deposit (*10*).

Atmospheric and astronomical observations. Generally similar atmospheric and astronomical imaging campaigns were conducted by both rovers during their 90-sol primary missions (*6*), except that nighttime imaging observations on Opportunity were precluded because of power limitations. Atmospheric observations include direct solar imaging, using 440- and 880-nm neutral-density filters, to derive and monitor the visible and near-IR dust opacity (*33*); time-lapse observations of sunsets to constrain the vertical distribution of atmospheric dust (Fig. 9); and

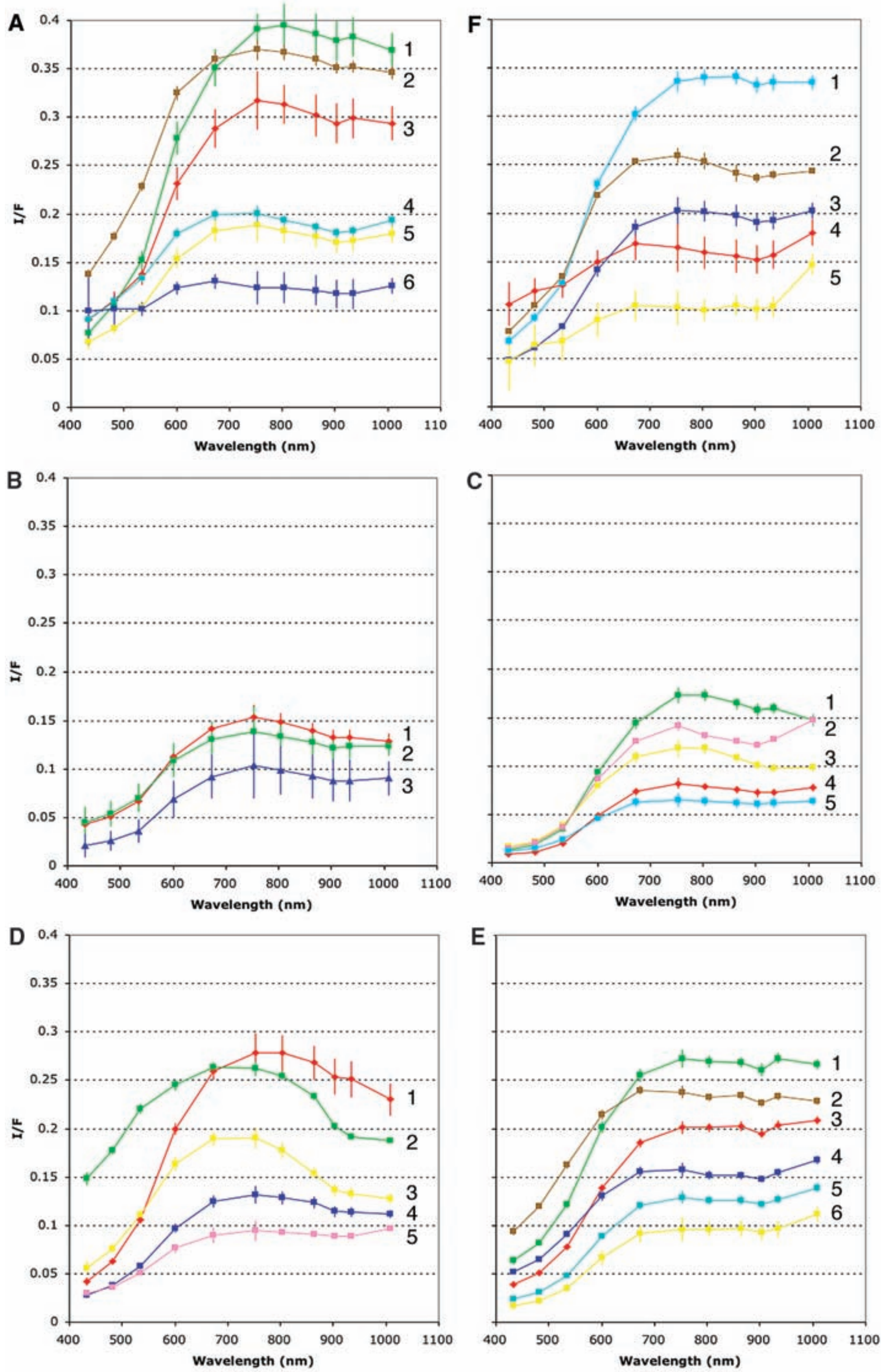

Fig. 8. Representative visible to near-IR Pancam spectra of units identified during Opportunity's primary mission. (**A**) to (**E**) correspond to locations shown in Fig. 7, A to E; (**F**) corresponds to spectra extracted from the following features in Plate 11A: (1) bright outcrop materials, (2) bright rock fragments, (3) dark outcrop material, (4) average of bright parts of spherules within the Berry Bowl, and (5) average of darker parts of spherules within the Berry Bowl.

special imaging campaigns designed to characterize the sky's diffuse illumination radiance field and to search for atmospheric water ice clouds. As of the end of the primary mission (areocentric longitude of the Sun ~24°, corresponding to early southern hemisphere autumn), no clouds were detected at the landing site in Meridiani, nor were any dust devils detected in targeted or serendipitous horizon imaging. Astronomical observations consisted of imaging of three solar transits by Phobos and one by Deimos to better constrain their orbital characteristics and orbital evolution histories (Fig. 10) (*34*).

Fig. 9. Sunset image acquired on sol 20 near 17:55 LTST with the Sun ~1° above the horizon. This is an enhanced color composite generated with Pancam's 750-, 530-, and 430-nm filters.

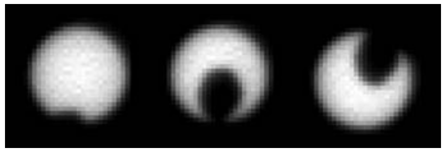

Fig. 10. Solar transit of Phobos observed on sol 47. Images taken through the Pancam right eye solar filter are shown at 10-s intervals, starting on the left, at 12 March 2004, 13:41:00 UTC.

References and Notes

1. P. R. Christensen *et al.*, *J. Geophys. Res.* **105**, 9623 (2000).
2. M. P. Golombek *et al.*, *J. Geophys. Res.* **108**, 10.1029/2003JE002074 (2003).
3. R. E. Arvidson *et al.*, *J. Geophys. Res.* **108**, 10.1029/2003JE001982 (2003).
4. Names have been assigned to aerographic features by the Mars Exploration Rover (MER) team for planning and operations purposes. The names are not formally recognized by the International Astronomical Union.
5. J. F. Bell III *et al.*, *J. Geophys. Res.* **108**, 10.1029/2003JE002070 (2003).
6. J. F. Bell III *et al.*, *Science* **305**, 800 (2004).
7. R. J. Reid *et al.*, *J. Geophys. Res.* **104**, 8907 (1999).
8. The term martian soil is used here to denote any loose unconsolidated materials that can be distinguished from rocks, bedrock, or strongly cohesive sediments. No implication of the presence or absence of organic materials or living matter is intended [e.g., (9)].
9. J. F. Bell III *et al.*, *J. Geophys. Res.* **105**, 1721 (2000).
10. R. E. Arvidson *et al.*, *Science* **306**, 1730 (2004).
11. S. W. Squyres *et al.*, *Science* **306**, 1709 (2004).
12. K. E. Herkenhoff *et al.*, *Science* **306**, 1727 (2004).
13. A martian solar day has a mean period of 24 hours 39 min 35.244 s and is referred to as a sol to distinguish this from a roughly 3% shorter solar day on Earth. A martian sidereal day, as measured with respect to the fixed stars, is 24 hours 37 min 22.663 s, as compared with 23 hours 56 min 04.0905 s for Earth. Local true solar time (LTST) on Mars is measured with respect to 24 "hours," with noon defined as the time when the Sun reaches its zenith in the sky. See www.giss.nasa.gov/tools/mars24 for more information.
14. R. Greeley, S. D. Thompson, *J. Geophys. Res.* **108**, 10.1029/2003JE002110 (2003).
15. R. Rieder *et al.*, *Science* **306**, 1746 (2004).
16. G. Klingelhöfer *et al.*, *Science* **306**, 1740 (2004).
17. L. A. Soderblom *et al.*, *Science* **306**, 1723 (2004).

18. An estimated albedo is derived by dividing *I/F* (determined from observations calibrated with the onboard calibration target) by the cosine of the solar elevation angle at the time of each observation. This albedo estimate should be comparable to the bolometric Lambert albedo values derived from orbital observations.
19. B. Hapke, *Theory of Reflectance and Emittance Spectroscopy* (Cambridge Univ. Press, New York, 1993).
20. J. R. Johnson *et al.*, *J. Geophys. Res.* **104**, 8809 (1999).
21. R. Greeley *et al.*, *Lunar Planet. Sci. Conf. XXXV*, abstr. 2162 (Lunar and Planetary Institute, Houston, TX, 2004) [CD].
22. R. V. Morris *et al.*, *Geochim. Cosmochim. Acta* **57**, 4597 (1993).
23. R. V. Morris *et al.*, *J. Geophys. Res.* **105**, 1757 (2000).
24. J. L. Bishop *et al.*, *J. Geophys. Res.* **103**, 31457 (1998).
25. R. V. Morris *et al.*, in *Mineral Spectroscopy: A Tribute to Roger G. Burns*, M. D. Dyar, C. McCammon, M. W. Schaefer, Eds. (Geochemical Society, Houston, TX, 1996), pp. 327–336.
26. R. V. Morris *et al.*, *J. Geophys. Res.* **100**, 5319 (1995).
27. R. V. Morris, D. C. Golden, *Icarus* **134**, 1 (1998).
28. P. R. Christensen *et al.*, *Science* **306**, 1733 (2004).
29. Both pyroxene and olivine exhibit broad Fe^{2+} absorption bands centered near 900 to 1100 nm [e.g., (*30*, *31*)], but because the long-wavelength sides of these bands are typically beyond the spectral range of silicon CCD detectors, it is usually not possible to uniquely identify the specific Fe^{2+}-bearing phases responsible for reflectance decreases observed in the longest wavelength filters of instruments such as Pancam (*32*).
30. J. B. Adams, *J. Geophys. Res.* **79**, 4829 (1974).
31. E. A. Cloutis *et al.*, *J. Geophys. Res.* **91**, 11641 (1986).
32. E. A. Cloutis, J. F. Bell III, *Icarus* **172**, 233 (2004).
33. M. T. Lemmon *et al.*, *Science* **306**, 1753 (2004).
34. J. F. Bell III *et al.*, in preparation.
35. We extend our sincere gratitude to the many hundreds of people who have contributed to the success of the Pancam investigation. These include the many MER engineers, managers, and support staffers at JPL; engineers and researchers at many vendor organizations; students and support staff at Cornell University, USGS/Flagstaff, Washington University, and other institutions; image processing and visualization experts at JPL and NASA/Ames Research Center; and many of the co-investigators, collaborators, and associates on the Athena Science Team. We also extend special thanks to our families and loved ones for their patience and support during mission operations and throughout the many years leading up to our spectacular travels on Mars.

Plates Referenced in Article
www.sciencemag.org/cgi/content/full/306/5702/1703/DC1
Plates 1, 2, 4 to 7, and 9 to 16

15 September 2004; accepted 15 October 2004

RESEARCH ARTICLE

In Situ Evidence for an Ancient Aqueous Environment at Meridiani Planum, Mars

S. W. Squyres,[1]* J. P. Grotzinger,[2] R. E. Arvidson,[3] J. F. Bell III,[1] W. Calvin,[4] P. R. Christensen,[5] B. C. Clark,[6] J. A. Crisp,[7] W. H. Farrand,[8] K. E. Herkenhoff,[9] J. R. Johnson,[9] G. Klingelhöfer,[10] A. H. Knoll,[11] S. M. McLennan,[12] H. Y. McSween Jr.,[13] R. V. Morris,[14] J. W. Rice Jr.,[5] R. Rieder,[15] L. A. Soderblom[9]

Sedimentary rocks at Eagle crater in Meridiani Planum are composed of fine-grained siliciclastic materials derived from weathering of basaltic rocks, sulfate minerals (including magnesium sulfate and jarosite) that constitute several tens of percent of the rock by weight, and hematite. Cross-stratification observed in rock outcrops indicates eolian and aqueous transport. Diagenetic features include hematite-rich concretions and crystal-mold vugs. We interpret the rocks to be a mixture of chemical and siliciclastic sediments with a complex diagenetic history. The environmental conditions that they record include episodic inundation by shallow surface water, evaporation, and desiccation. The geologic record at Meridiani Planum suggests that conditions were suitable for biological activity for a period of time in martian history.

The primary objective of the Mars Exploration Rover mission is to search for evidence in the martian geologic record of environmental conditions that might once have been suitable for life. Elsewhere in this issue (*1*) we describe the geologic setting in and around Eagle crater (*2*), the small impact crater in Meridiani Planum where the rover Opportunity landed. Here, we describe rocks exposed in the wall of Eagle crater in more detail and consider their implications for past aqueous processes and habitability.

Stratigraphy and sedimentology. The outcrop at Eagle crater can be mapped (Fig. 1) on the basis of color, morphology, texture, and structural attitude revealed in Pancam images (*3*). The maximum stratigraphic thickness exposed at any location within the outcrop is about 30 to 50 cm. Although the units we have mapped reveal a complex stratigraphy, intense brecciation associated with the impact event hinders reconstruction of the relative ages. Postdepositional surface weathering and collapse may also have contributed to brecciation.

The western part of the outcrop forms map unit A and includes an area called Shoemaker's Patio up to the point marked by the Slickrock fault. This unit is characterized by large breccia blocks and by the highest albedo (~0.30) within the outcrop when viewed in bulk. Bedding within blocks shows dips of 0° to 15°, defined by fine planar lamination, low-angle cross-stratification, and cross-bed sets as thick as 7 cm (Fig. 2A). Embedded spherules are present, but vugs are rare to absent. The margins of some breccia blocks show rims with raised relief and redder colors (*3*).

Map unit B, extending from the Slickrock fault northeastward toward the rock called El Capitan, is characterized by large blocks that are lower in albedo than those in map unit A. Bedding within the blocks is steep on the east side of the fault, with dips up to 60° as observed at Slickrock and a rock called the Dells. Bedding within unit B is characterized by planar lamination to low-angle cross-stratification (Fig. 2B), ripple cross-lamination (Plate 7), and crinkly to undulatory lamination (Fig. 2C). Embedded spherules and vugs are abundant.

Map unit C includes El Capitan and other rocks along the northern and outer margin of Eagle crater. Bedding planes are nearly horizontal, and bedding is more poorly expressed than elsewhere. In the upper part of El Capitan (Guadalupe), the bedding is only faintly visible. Embedded spherules are present and vugs are abundant. The upper part of

[1]Department of Astronomy, Cornell University, Ithaca, NY 14853, USA. [2]Department of Earth, Atmospheric, and Planetary Sciences, Massachusetts Institute of Technology, Cambridge, MA 02139, USA. [3]Department of Earth and Planetary Sciences, Washington University, St. Louis, MO 63031, USA. [4]Department of Geological Sciences, University of Nevada, Reno, NV 89557, USA. [5]Department of Geological Sciences, Arizona State University, Tempe, AZ 85287, USA. [6]Lockheed Martin Corporation, Littleton, CO 80127, USA. [7]Jet Propulsion Laboratory, California Institute of Technology, Pasadena, CA 91109, USA. [8]Space Science Institute, Boulder, CO 80301, USA. [9]U.S. Geological Survey, Flagstaff, AZ 86001, USA. [10]Johannes Gutenberg University, D-55128 Mainz, Germany. [11]Botanical Museum, Harvard University, Cambridge, MA 02138, USA. [12]Department of Geosciences, State University of New York, Stony Brook, NY 11794, USA. [13]Department of Earth and Planetary Sciences, University of Tennessee, Knoxville, TN 37996, USA. [14]NASA Johnson Space Center, Houston, TX 77058, USA. [15]Max-Planck-Institut für Chemie, Kosmochemie, D-55128 Mainz, Germany.

*To whom correspondence should be addressed. E-mail: squyres@astrosun.tn.cornell.edu